# Pulsed fusion space propulsion

## Computational Magneto-Hydro Dynamics of a multi-coil parabolic reaction chamber

Romanelli, G; Mignone, Andrea; Cervone, Angelo

**DOI**
10.1016/j.actaastro.2017.07.045

**Publication date**
2017

**Document Version**
Accepted author manuscript

**Published in**
Acta Astronautica

**Citation (APA)**
Romanelli, G., Mignone, A., & Cervone, A. (2017). Pulsed fusion space propulsion: Computational Magneto-Hydro Dynamics of a multi-coil parabolic reaction chamber. *Acta Astronautica*, *139*, 528-544. https://doi.org/10.1016/j.actaastro.2017.07.045

Postprint of Acta Astronautica
Volume 139, October 2017, Pages 528-544
Link to formal publication (Elsevier): https://doi.org/10.1016/j.actaastro.2017.07.045

# Pulsed Fusion Space Propulsion: Computational Magneto-Hydro Dynamics of a Multi-Coil Parabolic Reaction Chamber☆

Gherardo Romanelli[a,1,*], Andrea Mignone[b], Angelo Cervone[a]

[a] *Department of Space Engineering, Delft University of Technology, Kluyverweg 1, 2629 HS Delft, The Netherlands*
[b] *Physics Department, University of Turin, Via Pietro Giuria, 1, 10125 Turin, Italy*

**Abstract**

Pulsed fusion propulsion might finally revolutionise manned space exploration by providing an affordable and relatively fast access to interplanetary destinations. However, such systems are still in an early development phase and one of the key areas requiring further investigations is the operation of the magnetic nozzle, the device meant to exploit the fusion energy and generate thrust. One of the last pulsed fusion magnetic nozzle design is the so called multi-coil parabolic reaction chamber: the reaction is thereby ignited at the focus of an open parabolic chamber, enclosed by a series of coaxial superconducting coils that apply a magnetic field. The field, beside confining the reaction and preventing any contact between hot fusion plasma and chamber structure, is also meant to reflect the explosion and push plasma out of the rocket. Reflection is attained thanks to electric currents induced in conductive skin layers that cover each of the coils, the change of plasma axial momentum generates thrust in reaction. This working principle has yet to be extensively verified and computational Magneto-Hydro Dynamics (MHD) is a viable option to achieve that. This work is one of the first detailed ideal-MHD analysis of a a multi-coil parabolic reaction chamber of this kind and has been completed employing PLUTO, a freely distributed computational code developed at the Physics Department of the University of Turin. The results are thus a preliminary verification of the chamber's performance. Nonetheless, plasma leakage through the chamber structure has been highlighted. Therefore, further investigations are required to validate the chamber design. Implementing a more accurate physical model (e.g. Hall-MHD or relativistic-MHD) is thus mandatory, and PLUTO shows the capabilities to achieve that.

*Keywords:* fusion rocket, computational MHD, magnetic nozzle

☆This paper was presented during the $67^{th}$ IAC in Guadalajara

*Corresponding author
*Email addresses:* gherardo.romanelli@gmail.com (Gherardo Romanelli), mignone@ph.unito.it (Andrea Mignone), a.cervone@tudelft.nl (Angelo Cervone)
[1]Present Address: Largo Venezia 24, 52100 Arezzo, Italy

Abbreviations: British Interplanetary Society (BIS), Constrained Transport (CT), Electro-Motive Force (EMF), High Resolution Shock Capturing (HRSC), Human Outer Planet Exploration (HOPE), International Astronautical Congress (IAC), Inertial Confinement Fusion (ICF), Inertial Electrostatic Confinement Fusion (IECF), Magnetic Confinement Fusion (MCF), Initial Mass in Low Earth Orbit (IMLEO), Magneto-Inertial Fusion (MIF), Magnetised Target Fusion (MTF), Magneto-Hydro Dynamics (MHD), Relativistic Magneto-Hydro Dynamics (RMHD), Specific impulse ($I_{sp}$), Total Variation Diminishing (TVD)

## 1. Introduction

After the Apollo programme was shut down, no man has ever travelled into space farther than Low Earth Orbit (LEO). Many are indeed the causes: despite political and economical reasons, and maybe a general lack of interest, manned space exploration still presents several known and unknown challenges we do not yet have the capabilities and experience to overcome. Nevertheless, scientific and technological objectives keep encouraging the interest that many different parties put in manned interplanetary travel [1, 2]. Besides, the effects space environment has on the human body are being thoroughly studied on board the ISS [3]. However, even for the nearest destination beyond the moon (e.g. Mars), extensive manned space exploration is still strongly burdened by the nowadays available propulsion systems. A rapid, affordable and efficient (i.e. capable of a high-payload capacity) access to deep space would indeed require systems with both high $I_{sp}$ ($> 10^3$s) and high thrust ($> 10^4$N), two characteristics one can hardly find together in any of the space propulsion concepts of today: specific impulse is usually increased at the expense of thrust [4, 5, 6].

The development of advanced space propulsion systems is therefore one necessary step to finally revolutionise space exploration. Nuclear power is a promising alternative, for the high energy density of its fuel is particularly attractive for rocket engines. Besides, taming nuclear fusion may be the only option we have to make a 1-year interplanetary round trip possible [5, 7, 8]. Interest in applications of fusion power has a long history behind and despite breakeven point may still be far to achieve for mankind, several space propulsion concepts have been investigated in the last half-century [9, 10, 11, 12, 13, 14, 15, 16].

One of the main concerns when discussing nuclear fusion is the way the reaction is ignited and preserved. The options discussed are many (i.e. ICF, IECF, MCF, MIF, MTF), however, Magneto-Inertial Fusion has been projected to give the smallest solution and is thus seen as the most favourable alternative for space propulsion applications [5, 12]. Discussing the state of the art of the subject is however far beyond the scope of this paper. The authors will thus limit to saying that the z-pinch reactor (mentioned in the next), is one MIF device recognised by many as the most suitable for rockets [5, 17, 13]. What will be hereby discussed, instead, is the way thrust can be generated in a fusion rocket.

Directly accelerating fusion plasma out of the rocket assures the highest propulsion efficiencies, but the extreme plasma temperatures (i.e. $\sim 10^8$°C) makes it impossible to use any conventional nozzle. Nevertheless, since plasma is an ionised gas, electromagnetic interactions can be exploited to drive it out of the rocket. A magnetic nozzle can thus be employed for the purpose. The device applies a magnetic field that surrounds the plasma after the fusion reaction, reacts to its expansion and prevents any contact with the structure of the spacecraft. Also, the field is designed in such a way that the nozzle can directly accelerate the plasma out of the rocket and generate thrust in reaction. It is argued that experiments involving magnetic nozzles should be developed in parallel with those of the fusion reactor as they are equally critical for the advancement of fusion propulsion [5].

Fusion rockets can be classified according to several design parameters, nonetheless, what is mostly relevant for what presented in this study is the distinction between steady-state and pulsed fusion rockets. The former continuously apply thrust accelerating the plasma through a magnetic nozzle which is shaped very much alike a De Laval nozzle, while the latter applies the magnetic field so that repeated fusion explosions are reflected to push the spacecraft. A magnetic nozzle of the second kind can be referred to as magnetic flux compression reaction chamber, and has first been proposed in 1971 by Winterberg [16]. The same concept was implemented by Bond et al. in the Daedalus project of the BIS [18] and, ever since, alternative reaction chambers have been

considered (e.g. see [14]). One of the latest chamber design, which this research has focused on, has been introduced by Thio et al. in [15], and its projected capabilities detailed by Adams et al. in [19] and by the NASA's Advanced Concept Office in [13] for the HOPE concept mission.

In general, a reaction chamber is shaped like a bowl open to the backside of the rocket and the fusion reaction is ignited within the chamber somewhere along its axis. Coaxial electric coils are placed along the surface of the chamber and used to generate the initial magnetic field (i.e. seed magnetic field) that fills the inside of the chamber. The key to the working principle in every reaction chamber is thus the interaction between the expanding plasma and the magnetic field: while the fraction of plasma that expands towards the open side of the chamber goes practically unaltered, what moves towards the chamber structure is affected by the applied magnetic field. Fusion plasma is a highly conductive material and its dynamical interaction with an externally applied magnetic field results in the generation of currents on its surface that prevent the external field to further penetrate it. As a result, the field is swept by the expanding plasma as explained in [20].

The operation of the reaction chamber is completed by an additional element that assures the magnetic field behaves like a spring which loads while the plasma expands and then pushes it back out of the rocket before it touches the chamber structure: a conductor wall placed between the coils and the location were plasma is ignited can be used for such a purpose (see Fig. 1.a). During plasma expansion, azimuthal eddy currents (i.e. in the off-plane direction in Fig. 1) are generated along the wall in reaction to the changing magnetic field, as well. Therefore, the field cannot be swept across the wall and is compressed between that and the expanding plasma (see Fig. 1.b and 1.c). Due to its solenoidal property, the amplitude of the field (and hence the magnetic pressure) increases. During this phase, part of the plasma energy is thus transferred to the field until the plasma expanding towards the chamber stops. When that happens, the system reacts and returns to its stable initial condition, plasma is pushed out of the open side of the chamber and a new reaction can be ignited (see Fig. 1.d). Therefore, thrust force is applied at every fusion pulse to keep the total axial momentum of the system rocket+plasma balanced. Best results are attained when the conductor wall has a parabolic section and the reaction is ignited at the focus of the parabola; in that case plasma is reflected along the axis of the chamber and propulsion efficiency can ideally be as high as 86.3% according to [15]

More recent reaction chamber concepts, like what discussed in [19] and [13], remove the conductor wall and replace it with conductive skin layers to cover each coil (see Fig. 2): Azimuthal eddy currents that assure the correct operation of the chamber are thus generated within these skin layers. This way, the view factor of the fusion reaction (i.e. the probability that any neutron released by the reaction does not collide with the nozzle structure) is increased and the overall mass of the chamber can be reduced [19]. Fig. 3 shows a 3D model of this type of chamber which takes the name of multi-coil parabolic reaction chamber.

Thio et al. computed the performance of a plasma jet driven MTF rocket equipped with a multi-coil parabolic chamber in [15]. Calculations are thereby based upon a quite detailed balance of all the energy transformations involved, but plasma dynamics is only assumed in accordance with the theoretical working principle and not extensively verified. On the other hand, a simplified elementary analysis of the plasma dynamics in a multi-coil parabolic reaction chamber is discussed in [19] and [13]. However, electromagnetic interactions are not thereby included, the computed accelerations are kept constant for the selected time step and an Euler method is then employed to integrate plasma trajectories. Hence, the accuracy and reliability of the results might not be of the highest. Nonetheless, as shown in [20], these two models do in fact agree in the results.

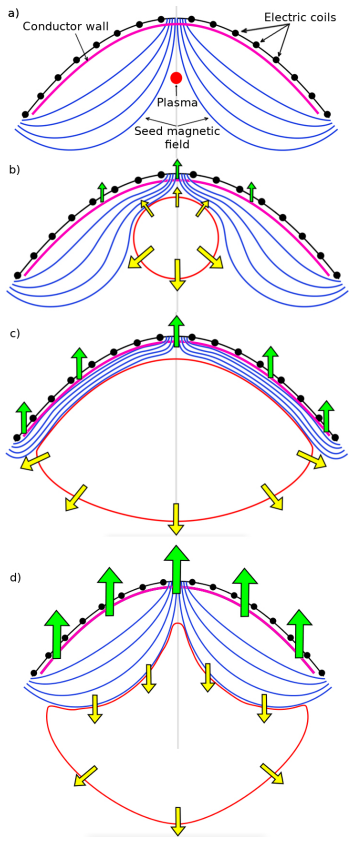


Figure 1: Schematic representation of how thrust (green arrows) is generated in a reaction chamber due to change of plasma momentum (yellow arrows)

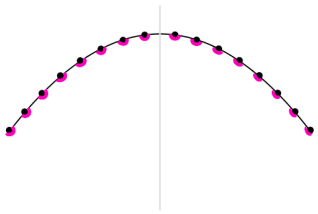

Figure 2: Section of a reaction chamber with conductive skin layers (purple) on the coils

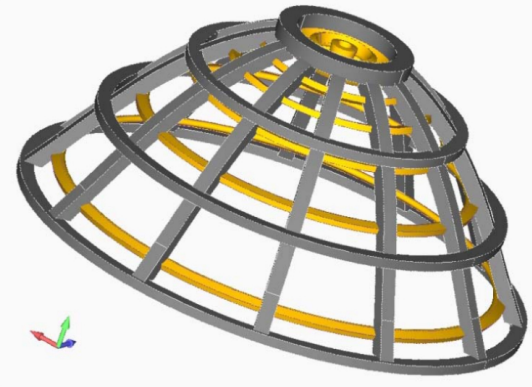

Figure 3: 3D model of a multi-coil parabolic reaction chamber (chamber structure (grey), electric coils (yellow) [13]

Before the specific chamber design and its estimated performance can be validated, plasma dynamics has to be thoroughly computed. Numerical simulations that apply advanced plasma physics models have a remarkable value and great effort has recently been put in developing sophisticated numerical codes that solve the plasma dynamics of complex propulsion systems [21, 22]. Nevertheless, the literature is still nowadays quite poor on the subject and this research has aimed to give a contribute to the subject.

Computational MHD aims to numerically solve the equations of MHD, one of the nowadays available models that describe plasma physics. One computational MHD analysis applied to a multi-coil parabolic reaction chamber is discussed by Stanic et al. in [23]. Nonetheless, the chamber design they use (i.e. number, geometry and arrangement of the coils) is derived from the study of Bond et al. [18] and a conductor parabolic wall is implemented in the model. The only other example is what the same authors of this paper included in [20], where the implemented conditions, though still reproducing a conductor parabolic wall, have been derived from the geometry and design discussed by Thio et al. in [15] and by Adams et al. in [19] and [13]. The analysis hereby presented is thus an improvement of what already discussed in [20] and does indeed include the effect of separate conductive skin layers. It is believed to be the so far most accurate reproduction of the reaction chamber concept proposed by Thio et al. and Adams et al., and it aims to contribute to the validation of the specific chamber design.

The results of this study are compared with the performance estimated through the simplified models of [15] and [13], which are reported in Table 1. There, 2 different cases are presented: the first shows the estimated performance of a plasma jet driven MTF rocket as discussed in [15] and [19], while the second of a Z-Pinch MIF rocket as discussed in [13]. Note that the chamber aperture angle of Case 1 has been purposely changed from 75 ° to 60.9 °. The 2 cases were selected among all the pulsed fusion reactor concepts because of the availability in the literature of complete calculations and data about their estimated performance. The authors of this paper do not claim these are the most promising devices for fusion propulsion. The aim of this study is only to test the validity of a multi-coil parabolic reaction chamber that attains plasma reflection due to electric currents induced in conductive skin layers covering each of its coils.

| | Case 1 | Case 2 |
|---|---|---|
| $m_0$[kg] | 0.002 | 0.02 |
| $e_f$[MJ] | 973 | 1,000 |
| $e_{th,0}$[MJ] | 905 | 584 |
| $f_{rep}$[Hz] | 200 | 10 |
| $f_l$[m] | 2 | 2 |
| $\theta_a$[°] | 60.9 | 60.9 |
| $\Delta p_z$[kg m/s] | $1.6 \cdot 10^3$ | $3.8 \cdot 10^3$ |
| $I_{sp}$[s] | $82 \cdot 10^3$ | $19 \cdot 10^3$ |
| $\eta$ | 0.81 | 0.60 |
| $T$[kN] | 320 | 38 |

Table 1: Initial conditions and estimated performance of the MTF rocket (Case 1) [15] and of the z-pinch space propulsion concept (Case 2) [13]

## 2. Computational code

All the simulations hereby reported have been completed with the aid of PLUTO[2] code. PLUTO is a freely-distributed and modular code for computational astrophysics, and what hereby presented shows that it can also be suitable for engineering applications. It has been developed by a team led by Prof. Andrea Mignone at the Physics Department of the University of Turin [24] and has been programmed to implement different physical models including ideal-, resistive- and relativistic-MHD.

The code is designed to integrate a set of non-linear hyperbolic conservation laws (i.e. Euler Equations [25]) of the kind expressed in Eq. (1) [24]:

$$\frac{\partial \boldsymbol{U}}{\partial t} = -\nabla \cdot \boldsymbol{F}(U) + \boldsymbol{S}(U). \tag{1}$$

PLUTO solves MHD equations in fully conservative form using high-resolution, Godunov-type, shock-capturing schemes, which have been proven to be reliable and robust for the modelling of supersonic flows [24]. Moreover, it employs a structured and rectangular mesh.

### *2.1. Physical model employed*

To complete this study, an ideal-MHD model has been applied, therefore, $\boldsymbol{S}(U) = 0$ in Eq. (1). The resulting laws are reported in Eqs. (2)-(5), where the conservation of mass, total momentum, total energy, and magnetic field, are respectively defined. The applied Ohm's Law is $\boldsymbol{E} = -\boldsymbol{v} \times \boldsymbol{B}$.

$$\frac{\partial \rho}{\partial t} + \boldsymbol{\nabla} \cdot (\rho \boldsymbol{v}) = 0; \tag{2}$$

$$\frac{\partial (\rho \boldsymbol{v})}{\partial t} + \boldsymbol{\nabla} \cdot \left( \rho \boldsymbol{v} \otimes \boldsymbol{v} + p_{tm} \boldsymbol{I} - \frac{\boldsymbol{B} \otimes \boldsymbol{B}}{\mu_0} \right) = 0; \tag{3}$$

[2] `http://plutocode.ph.unito.it`

$$\frac{\partial e_{tot}}{\partial t} + \boldsymbol{\nabla}\cdot\left[\boldsymbol{v}\left(e_{tot} + p_{tm}\right) - \frac{(\boldsymbol{v}\cdot\boldsymbol{B})\boldsymbol{B}}{\mu_0}\right] = 0; \tag{4}$$

$$\frac{\partial \boldsymbol{B}}{\partial t} + \boldsymbol{\nabla}\cdot(\boldsymbol{v}\otimes\boldsymbol{B} - \boldsymbol{B}\otimes\boldsymbol{v}) = 0. \tag{5}$$

The total energy ($e_{tot}$), the thermal energy ($e_{th}$) and the thermo-magnetic pressure ($p_{tm}$) can respectively be defined as in Eqs. (6)-(8).

$$e_{tot} = \frac{\rho v^2}{2} + e_{th} + \frac{B^2}{2\mu_0}; \tag{6}$$

$$e_{th} = \frac{p_h}{\gamma - 1}; \tag{7}$$

$$p_{tm} = p_h + \frac{B^2}{2\mu_0}. \tag{8}$$

The integration has been carried out with a $2^{nd}$ order TVD Runge-Kutta algorithm, and the solenoidal property of the magnetic field maintained using a CT strategy. Indeed, as Mignone discussed in [24], this method is capable of maintaining the divergence-free condition at machine accuracy. The results hereby reported have been attained using version 4.2 of the code compiled on Arch Linux 4.10 running on an Asus laptop equipped with an Intel® Core™ i5-2410M. In addition, the included plots have been produced with the aid of VisIt 2.12 [26].

## 3. Analysis set-up

In this study, the fusion reaction has been assumed completed, already, and no further verifications and explanation of the ignition process are included. Hence, the computation starts with a spherical plasma pellet of radius $R_0$ centred in the focal point of the chamber. Its initial velocity has been assumed equal to 0, and its thermal energy derived from [15] and [13]. The physical properties of the plasma at time $t = 0$ are thus reported in Table 2. $R_0$ has been selected to have an accurate reproduction of the plasma with the chosen mesh resolution.

For computational reasons, the complexity of the problem has been reduced by using axisymmetric cylindrical coordinates ($r$, $z$). The physical model is therefore invariant for rotation around the vertical axis although all 3 vector components are evolved in time. Fig. 4 shows half a section of the parabolic chamber with the distribution of the 8 electric coils and the spherical plasma in its initial conditions.

The location of the electric coils and the respective applied current (see Table 3) have been derived from [13] (i.e. Case 2) as other studies lack this kind of information. However, as the energy of the expanding plasma (i.e. $e_{th,0}$) is different in the 2 cases, the currents of Case 2 have been corrected for Case 1 according to Eq. (9) which has been derived from the relation $I^2_{case1}/I^2_{case2} \propto B^2_{case1}/B^2_{case2} \propto e_{th.0,case1}/e_{th.0,case2} = 1.54$.

$$I_{case1} = \sqrt{1.54}\cdot I_{case2}. \tag{9}$$

| | Case 1 | Case 2 |
|---|---|---|
| $m_0$[kg] | 0.002 | 0.02 |
| $R_0$[m] | 0.3 | 0.3 |
| $e_{th,0}$[MJ] | 905 | 584 |
| $v_0$[m/s] | 0.0 | 0.0 |

Table 2: Plasma initial conditions [19]

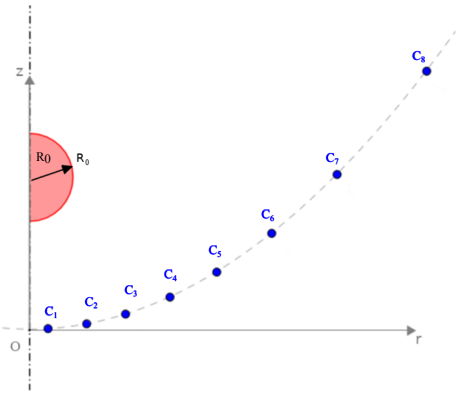


Figure 4: Geometrical definition of the multi-coil reaction chamber, with $z = r^2/(4f_l)$ and $f_l = 2\,\mathrm{m}$

### *3.1. Computational domain*

The size of the domain has been set to fully include the maximum radius of the chamber and leave room for a reasonable expansion of the plasma in the axial direction. Hence, it extends from 0 to 8.1 m in the $r$-direction and from 0 to 15.75 m in the $z$-direction.

Table 4 shows the properties of the computational domain including the implemented boundary conditions. Across the axis $r = 0$, where an *axisymmetric* condition is imposed, all scalar variables $q$ are symmetrised (i.e. $q \to q$) and the sign of both radial and azimuthal vector components are flipped (i.e. $v_{r;\phi} \to -v_{r;\phi}$ and $B_{r;\phi} \to -B_{r;\phi}$). The *outflow* condition leaves all the variables unchanged across the remaining boundaries (i.e. their spatial gradient in the normal direction to the domain border is set equal to $0 \Rightarrow \partial q/\partial\hat{n} = \partial\boldsymbol{v}/\partial\hat{n} = \partial\boldsymbol{B}/\partial\hat{n} = 0$).

### *3.2. Seed magnetic field*

In order to ensure the divergence-free condition, the seed magnetic field generated by the electric coils has been initialized using the vector potential and its field components derived according to Eq. (10).

$$\boldsymbol{B} = \nabla \times \boldsymbol{A}. \tag{10}$$

An exact solution of the vector potential related to the field generated by a current coil is not yet available. Nonetheless, an approximate solution that makes use of the first and second complete elliptic integrals (i.e. $K(k^2)$ and $E(k^2)$, respectively) has been found in the literature [27, 28, 29].

| Case 1 | | | | |
|---|---|---|---|---|
| | $c_1$ | $c_2$ | $c_3$ | $c_4$ |
| $I_0\,[10^5\mathrm{A}]$ | 313.0 | 51.2 | 24.1 | 14.5 |
| $r_n\,[cm]$ | 27.8 | 84.4 | 144.0 | 211.0 |
| $z_n\,[cm]$ | 0.96 | 8.9 | 26.1 | 55.6 |
| | $c_5$ | $c_6$ | $c_7$ | $c_8$ |
| $I_0\,[10^5\mathrm{A}]$ | 9.66 | 6.72 | 4.72 | 3.26 |
| $r_n\,[cm]$ | 288.0 | 382.0 | 505.0 | 681.0 |
| $z_n\,[cm]$ | 104.0 | 182.0 | 319.0 | 579.0 |
| Case 2 | | | | |
| | $c_1$ | $c_2$ | $c_3$ | $c_4$ |
| $I_0\,[10^5\mathrm{A}]$ | 252.0 | 41.3 | 19.4 | 11.7 |
| $r_n\,[cm]$ | 27.8 | 84.4 | 144.0 | 211.0 |
| $z_n\,[cm]$ | 0.96 | 8.9 | 26.1 | 55.6 |
| | $c_5$ | $c_6$ | $c_7$ | $c_8$ |
| $I_0\,[10^5\mathrm{A}]$ | 7.79 | 5.42 | 3.81 | 2.63 |
| $r_n\,[cm]$ | 288.0 | 382.0 | 505.0 | 681.0 |
| $z_n\,[cm]$ | 104.0 | 182.0 | 319.0 | 579.0 |

Table 3: Electric coil specifications [13]

Hence, with $k^2$ defined by Eq. (11), the azimuthal component of the vector potential $\boldsymbol{A}_\phi(r,z)$ can be defined as in Eq. (12). As a result, all magnetic field components are entirely contained in the plane of integration.

$$k^2 = \frac{4a_n r}{a_n^2 + r^2 + (z-z_n)^2 - 2a_n r}, \tag{11}$$

$$\begin{aligned} A_\phi(r,z) =& \frac{4Ia_n}{c\sqrt{a_n^2 + r^2 + (z-z_n)^2 - 2a_n r}} \times \\ & \times \left[ \frac{(2-k^2)\,K(k^2) - 2E(k^2)}{k^2} \right]. \end{aligned} \tag{12}$$

The vector potential related to each electric coil has thus been attained in each computational cell from the linear interpolation of tabulated values of the square bracket of Eq. (12) as a function of $k^2$. The contribution of every coil has then been summed up to compute the seed magnetic field of the chamber. The result related to Case 1 is shown in Fig. 5, where the coordinates are in code

| | size [m] |
|---|---|
| $r$ | 8.1 |
| $z$ | 15.75 |
| | resolution |
| $r$ | 280 |
| $z$ | 560 |
| | boundary conditions |
| $r = 0$ | axisymmetric |
| $r = 810\,\mathrm{cm}$ | outflow |
| $z = 0$ | outflow |
| $z = 1575\,\mathrm{cm}$ | outflow |

Table 4: Computational domain definition

units, the coloured profile expresses the magnetic field magnitude in Gauss ($1\,G = 10^{-4}\,T$), and the field lines have been included.

To then emulate the effect of the conductive skin layers of the coils, the temporal evolution of the magnetic field has been frozen in a number of cells around the coordinates of each coil (i.e. $(r_n, z_n)$): the azimuthal component of the EMF $\mathcal{E}_\phi$ has been constrained to be constant and identically equal to 0 within those cells for the total integration time. The cells identified for this purpose have been those having the geometrical centre located within a specific radial distance from the coordinates $(r_n, z_n)$; the radial distance has been selected to be comparable to the minor radius of each coil (i.e. $\sim 15\,\mathrm{cm}$ according to [13]). The strategy the code then employs to compute the temporal evolution of the magnetic field assures that the EMF (including its out-of-plane component $\mathcal{E}_\phi$) is updated in the rest of the domain to maintain the solenoidal condition of the field at machine accuracy. As a result, the magnetic field cannot be pushed across the selected cells and the projected operation of the reaction chamber is reproduced.

Moreover, the code has been instructed to not update physical quantities in those same cells. This approach has the advantage of limiting numerical issues caused by the computation of relativistic Alfvén speeds (not properly handled by the ideal-MHD model implemented). Due to the mathematical definition used for the magnetic field, extremely large field magnitudes (i.e. $\sim 100\,\mathrm{T}$) are indeed attained close to the origin of the field (i.e. $(r_n, z_n)$). Therefore, since Alfvén speed ($v_A$) is computed in each cell according to to Eq. (13), low ambient densities (i.e. $\sim 10^{-10}\,\mathrm{g/cm^3}$) implemented to reproduce deep space vacuum conditions can cause values of $v_A \simeq c$.

$$v_A = \sqrt{\frac{B^2}{\mu_0 \rho}}. \tag{13}$$

*3.3. Ambient conditions*

The rocket hereby examined is meant to operate in deep space vacuum conditions which, according to [30], can show pressure and particle density as low as $10^{-12}\,\mathrm{mbar}$ and $10\,\mathrm{cm^{-3}}$ (i.e.

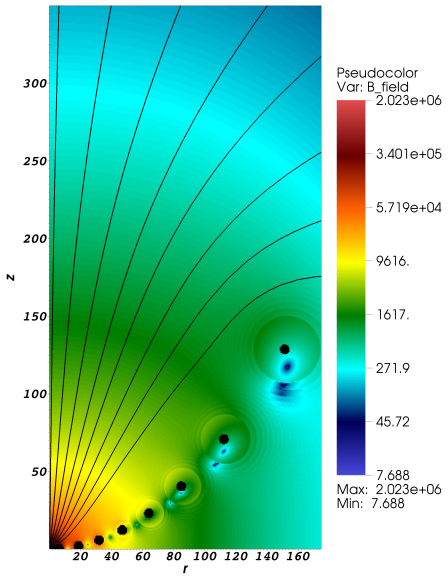


Figure 5: Case 1: Initial seed magnetic field magnitude [*Gauss*] and field lines ($t = 0$)

$\rho \simeq 10^{-23}\,\mathrm{g/cm^3}$), respectively. However, implementing such extreme conditions with an ideal-MHD model would cause numerical issues (i.e. relativistic Alfvén speeds), an excessive reduction of the integration time-step and hence make the solution impractical.

On one hand, minimum ambient density that can be set is limited by Eq. (13) in order to not attain $v_A \geq c$. Therefore, since magnetic fields $\sim 100\,\mathrm{T}$ are computed in the domain, minimum ambient density is $\sim 10^{-10}\,\mathrm{g/cm^3}$. Nonetheless, due to the restricted computational power employed, this limit has been further increased to maintain total computational time within reasonable limits. Ambient pressure, on the other hand, has been kept to levels that would prevent too strong and frequent shock waves to occur, again, to limit the computational effort required. Besides, further decreasing ambient pressure has been found not having noticeable effects on the computed plasma dynamics: magnetic pressure has hereby the dominant effect. As a result, the eventually implemented conditions are $p_h = 30.0\,\mathrm{mbar}$ and $\rho = 2.0 \cdot 10^{-9}\,\mathrm{g/cm^3}$.

### *3.4. Runtime Analysis*

The change of plasma axial momentum has been selected as the reference parameter to estimate the performance of the reaction chamber. However, the variation of plasma momentum is affected by the interaction with the externally applied magnetic field, on one side, and by the resistance ambient matter applies, on the other: part of plasma energy is indeed spent to push ambient matter out of the chamber. Hence, an effort has been put to limit the contribution of this latter aspect on the computed performance, and to correctly keep track of the plasma dynamics, a tracer (i.e. $\mathcal{T}$) has been added to the initial conditions using the relation of Eq. (14). The plasma initially located above the line that passes through the focus of the parabola and the $8^{th}$ electric coil has thus been excluded from the analysis. That is in fact the portion of plasma that interacts the least with the seed magnetic field and is affected the most by the implemented ambient conditions. The

computed nozzle efficiency of the chamber was indeed 3% lower in simulations were this portion of plasma was not excluded.

$$\mathcal{T} = \begin{cases} 1 & \text{if} \quad \begin{cases} \sqrt{r^2+z^2} \leq R_0 \\ z < \frac{z_8 - f_l}{r_8} r + f_l \end{cases} \\ 0 & \text{otherwise.} \end{cases} \tag{14}$$

Furthermore, as the plasma mixes with ambient matter during its expansion, the value of $\mathcal{T}$ evolves in each computational cell between 0 and 1 according to the percentage of mixing. Therefore, $\mathcal{T}$ has been employed as a weighting factor to estimate the total plasma axial momentum at every new integration step using the relation defined in Eq. (15), where the contribution of each computational cell $i$ has been summed.

$$\Delta p_z = \sum_i \mathcal{T}_i \rho_i v_{z,i} V_i. \tag{15}$$

Hence, the $I_{sp}$, the nozzle efficiency and average thrust have been respectively computed as expressed in Eqs. (16)-(18).

$$I_{sp} = \frac{\Delta p_z}{m_0 g_0}; \tag{16}$$

$$\eta_j = \frac{\Delta p_z}{\sqrt{m_0 2 e_f}}; \tag{17}$$

$$T = \Delta p_z f_{rep}. \tag{18}$$

## 4. Results and discussion

The analysis hereby described has been sufficient to complete a preliminary verification of a multi-coil parabolic reaction chamber that implements each of its electric coil covered by an additional conductive skin layer. The results of the computed plasma dynamics are shown in AppendixA where several snapshots taken at different integration times are included. By comparing the results of this analysis (see Table 5) with what from previously estimated performance (see Table 1), some notes have been derived.

Despite some possible numerical inaccuracies, the difference of computed performance with respect to reference values has been attributed to the not yet completely negligible effect of non-vacuum ambient conditions implemented, on one side, and to some plasma leakage through the chamber structure, on the other.

Ambient pressure has been reduced to a point at which its contribution to thermo-magnetic pressure $p_{tm}$ is negligible: results do not show variations if repeated with lower values of ambient pressure as $p_m$ has hereby the dominant effect. However, ambient density could not be further

| | Case 1 | Case 2 |
|---|---|---|
| $t_f$ [µs] | 14 | 42 |
| $\Delta p_z$ [kg m/s] | $1.2 \cdot 10^3$ | $3.4 \cdot 10^3$ |
| $I_{sp}$ [s] | $61 \cdot 10^3$ | $19 \cdot 10^3$ |
| $\eta_j$ | 0.60 | 0.58 |
| $T$ [kN] | 238 | 33 |

Table 5: Results of the computational analysis

decreased due to the already discussed limitations of the applied method and, especially in Case 1 where initial plasma mass is 10 times lower than Case 2, that is still believed to obstruct too much plasma dynamics.

On the other hand, plasma leakage, highlighted in both Case 1 and 2, is particularly important between the $6^{th}$, $7^{th}$ and $8^{th}$ electric coil and can arguably be interpreted in different ways:

- The initial seed magnetic field is too weak around that location;
- The coil spacing is too wide;
- The leakage is due to numerical resistivity.

To support the first argument of the list, a solution of Case 1 has been completed implementing a field twice as strong. The results are shown in Fig. 6 where the profile of $\mathcal{T} \cdot \rho$ at time $t = 14\,\mu s$ is presented together with the electric coils marked in black (spatial coordinates are expressed in code units). The plot on top is relative to the reference case, while the one on the bottom has been attained using a current twice the value of Table 2. The solution on top does show some plasma leakage through the last two coils, while the other does not highlight considerable leakages. Hence, a stronger magnetic field might decrease the aforementioned issue.

Coil spacing does also get quite wide towards the exit of the nozzle, and that might as well be cause of the leakage. To check this possibility solution of Case 1 has been repeated adding a $9^{th}$ coil such that $I_{0,9} = I_{0,8} \cdot I_{0,8}/I_{0,7}$, and the last 3 coils have been rearranged to reduce the interstice between them. The result can be seen in Fig. 7 where the profile of $\mathcal{T} \cdot \rho$ is again showed and leakages do indeed seem reduced.

Concerning numerical resistivity, as mentioned in [23] that can have an effect analogous to what of natural plasma resistivity. Hence, it may cause a transversal penetration of the plasma through the magnetic field, and the pointed out leakage, as a consequence. Besides, field penetration is indeed highlighted in the plots in AppendixA (see the black field lines). Numerical resistivity can be reduced by increasing the grid resolution, however, as far as the computational power of the employed machine would allow, higher resolutions did not highlight a considerable reduction of the leakage.

Another interesting aspect that has been noted is the shape the plasma assumes during its reflection. This suggests that the use of separate coils may not assure a parabolic reflection as the magnetic field between two consecutive coils deforms too much from the expected parabolic configuration. This issue is highlighted in Fig. 8 where the magnetic field lines have been added to the same $\mathcal{T} \cdot \rho$ profile of Case 1. The plots show two moments of plasma expansion. Closer to the parabola vertex the coil spacing is narrow enough for the magnetic field to assume a parabolic

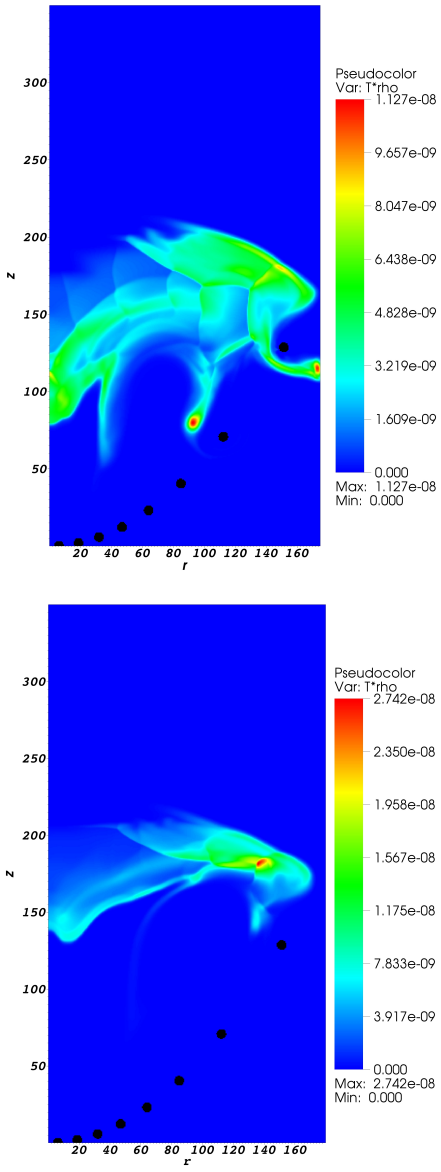


Figure 6: Case 1: $\mathcal{T} \cdot \rho$ profile at $t = 14\,\mu\text{s}$ for $I_0 = I_0$ (top) and $I_0 = 2 \cdot I_0$ (bottom)

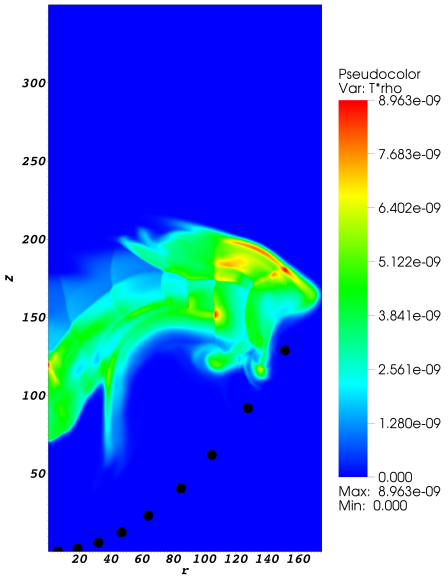


Figure 7: Case 1: $\mathcal{T} \cdot \rho$ profile at $t = 14\,\mu s$ with the addition of a $9^{th}$ coil

shape (top plot), while closer to the exit (bottom plot) the field deforms in an undesirable manner, part of the plasma leaks and is there trapped.

To further investigate this aspect, calculations have been completed again by implementing a parabolic conductor wall. Therefore, following the same approach discussed in Section 3.2 the magnetic field has been frozen in all the cells of the domain having the geometrical centre located within an area defined by the relation expressed in Eq. (19) and with a positive $z_{offset}$ selected to quite accurately reproduce the conductor wall. Snapshots of the simulation are reported in AppendixB. Images clearly show the magnetic field assumes a parabolic shape and Fig. 9 can be used to compare the computed conditions with what from Fig. 8. No leakage is highlighted and propulsion efficiency is indeed 5% higher when a conductor wall is implemented in the model. Therefore, it appears that the assets of a parabolic chamber can fully be exploited only when eddy currents are generated along a continuous parabolic section (i.e. a conductor wall), or when the inter-spacing between the coils covered by a conductive skin layer is correctly selected.

$$\begin{cases} z < r^2/(4f_l) + z_{offset} \\ z < 134. \end{cases} \tag{19}$$

### *4.1. Conclusion*

What hereby presented is the first computational analysis of the plasma dynamics in a multi-coil parabolic reaction chamber that implements electric coils each covered by a conductive skin layer. Previous analyses, like [23] and [20], included the effect of a conductor wall, instead. Despite the obvious incompleteness of this study, the effort that has been put in the mathematical definition

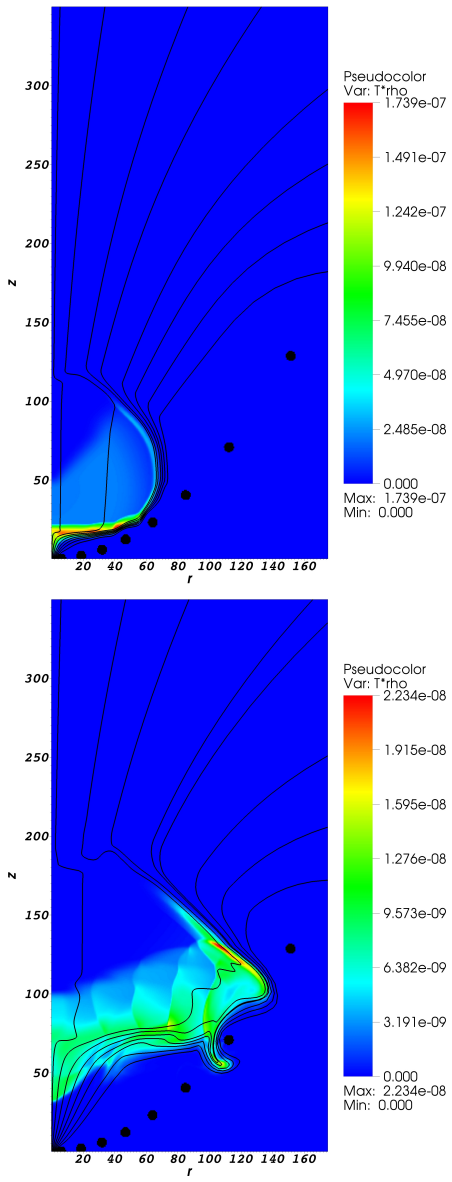


Figure 8: Case 1: $\mathcal{T} \cdot \rho$ profile and magnetic field lines at $t = 2.8\,\mu s$ (top) and at $t = 8.4\,\mu s$ (bottom)

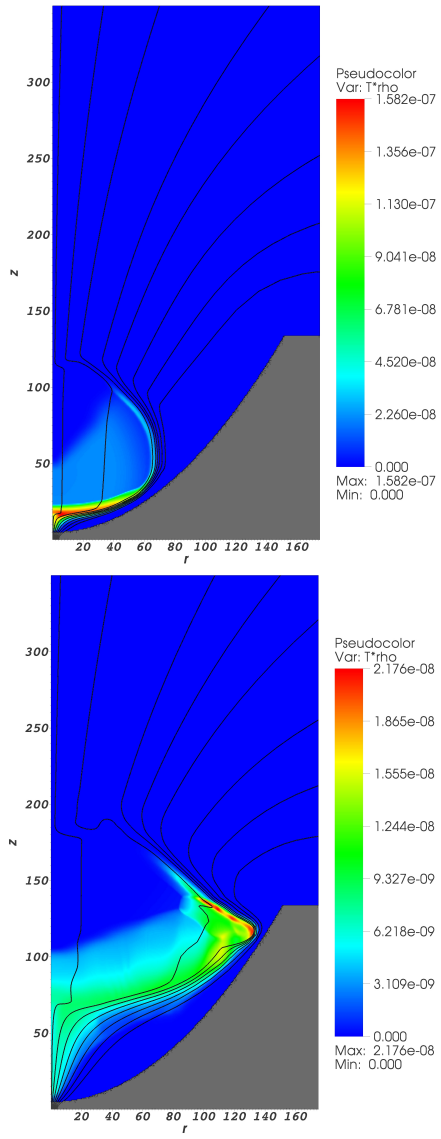


Figure 9: Case 1 with conductor wall: $\mathcal{T} \cdot \rho$ profile and magnetic field lines at $t = 2.8\,\mu s$ (top) and at $t = 8.4\,\mu s$ (bottom)

of the magnetic field and in the implementation of the electric coils in the domain is still believed could bring an important contribute to the discussed subject. The general operation of the reaction chamber in both Case 1 and 2 has been reproduced and plasma reflection achieved. However, the suitability of a multi-coil reaction chamber for space propulsion application has yet to be fully demonstrated. In particular, the highlighted plasma leakage has to be further investigated to understand if it could indeed compromise the suitability of separate conductive skin layers.

The ideal-MHD model employed for this study may lack in reliability and accuracy as it does not include some important aspects of plasma physics. That is particularly valid for what it concerns the Ohm's Law implemented in the model. In fact, recent parametric analyses (e.g. [31] and [22]) highlighted that including the Hall effect term is indeed necessary to model fusion plasma dynamics more correctly. Effects of finite resistivity should also be further investigated [32]. A resistive-MHD model is already included in PLUTO and Hall-MHD has been planned to be soon implemented in an official update.

This analysis has also investigated the effect of non-perfect vacuum conditions implemented in the problem. For what it concerns the ambient pressure, that can conveniently be reduced to a level its effect on the overall plasma dynamics is negligible with respect to the magnetic pressure applied by the field: this suggests that it may not be necessary to further decrease it. On the other hand, reducing ambient density is mandatory to thoroughly estimate the chamber's performance. To achieve that, a more robust MHD model is necessary, and a RMHD may show the right capabilities to do so. A RMHD (already included in PLUTO) has indeed a more rigorous control over all plasma signal velocities (e.g. Alfvén speed) which, thanks to a specific routine, are constrained to non-superluminal values. The stability of the numerical analysis would thus be greatly increased. Preliminary simulations completed have proven this aspect.

In addition, the accuracy of the implemented model can still be increased. A 2-dimensional and axisymmetric solution does not take in consideration several aspects pf plasma physics and instabilities that might change the overall dynamics of the chamber. Therefore, completing a 3-dimensional solution may of course provide more reliable and instructive results. Additional insights may be achieved with the implementation of non-ideal initial conditions (e.g. non-spherical plasma) and non-ideal equation of state to better reproduce the thermodynamics of the expanding plasma. PLUTO has nonetheless shown it might have the capabilities to complete all these tasks.

**Acknowledgements**

This research did not receive any specific grant from funding agencies in the public, commercial, or not-for-profit sectors. What hereby included follows the master's thesis project completed by the corresponding author and presented at the $67^{th}$ International Astronautical Congress (IAC) held in Guadalajara. Special thanks thus go to the Space Systems Engineering department of the Delft University of Technology, and to the session chairs of the IAC who selected this paper for the peer-review of this publication.

## AppendixA. Case 1: snapshots

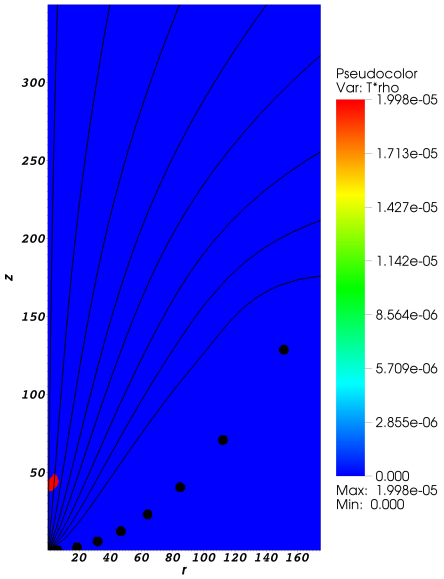


Figure A.10: $\mathcal{T} \cdot \rho$ profile and magnetic field lines at $t = 0\,\mu s$

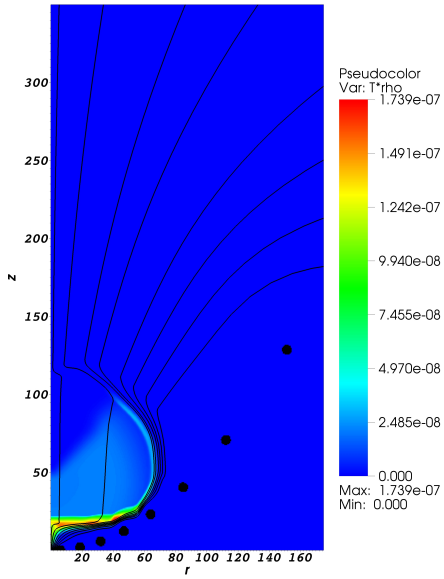


Figure A.11: $\mathcal{T} \cdot \rho$ profile and magnetic field lines at $t = 2.8\,\mu s$

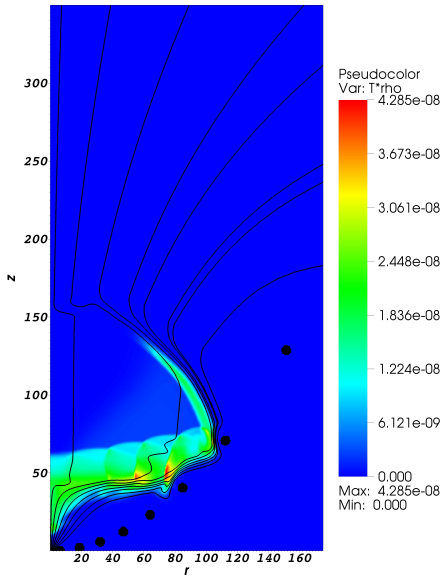


Figure A.12: $\mathcal{T} \cdot \rho$ profile and magnetic field lines at $t = 5.6\,\mu\text{s}$

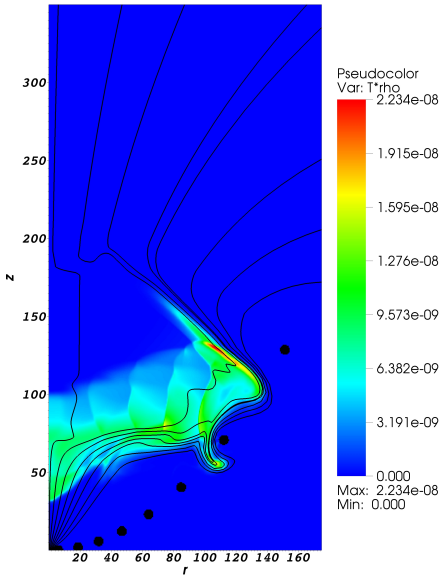


Figure A.13: $\mathcal{T} \cdot \rho$ profile and magnetic field lines at $t = 8.4\,\mu\text{s}$

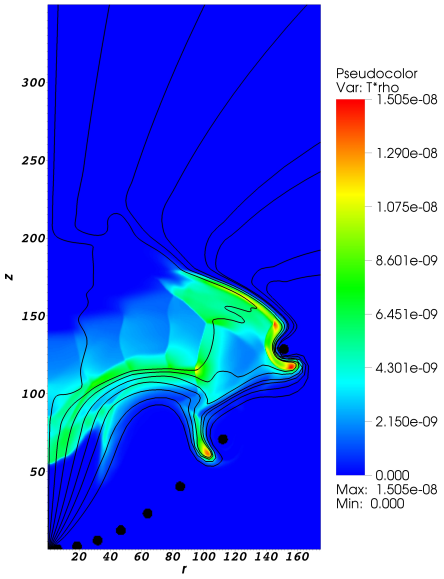


Figure A.14: $\mathcal{T} \cdot \rho$ profile and magnetic field lines at $t = 11.2\,\mu s$

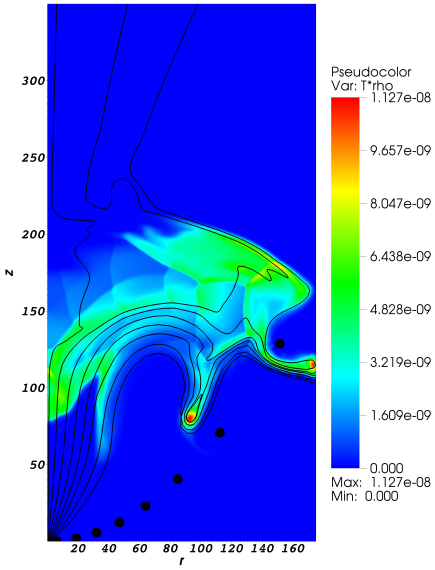


Figure A.15: $\mathcal{T} \cdot \rho$ profile and magnetic field lines at $t = 14\,\mu s$

## AppendixB. Case 1 with conductor wall: snapshots

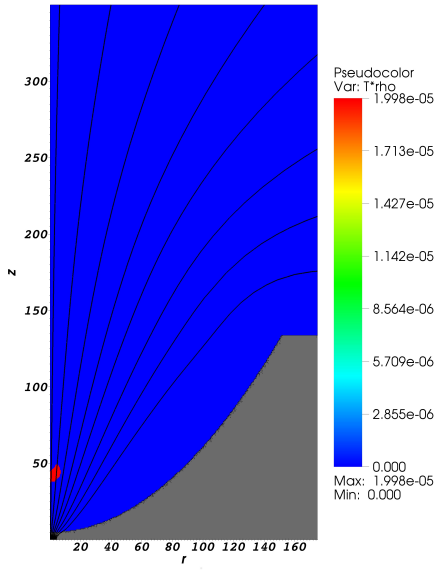


Figure B.16: $\mathcal{T} \cdot \rho$ profile and magnetic field lines at $t = 0\,\mu s$

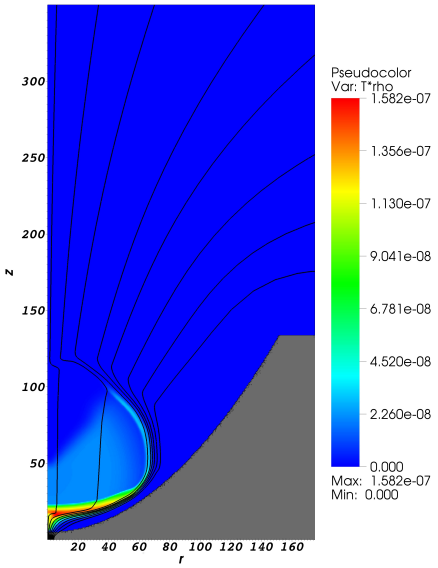


Figure B.17: $\mathcal{T} \cdot \rho$ profile and magnetic field lines at $t = 2.8\,\mu s$

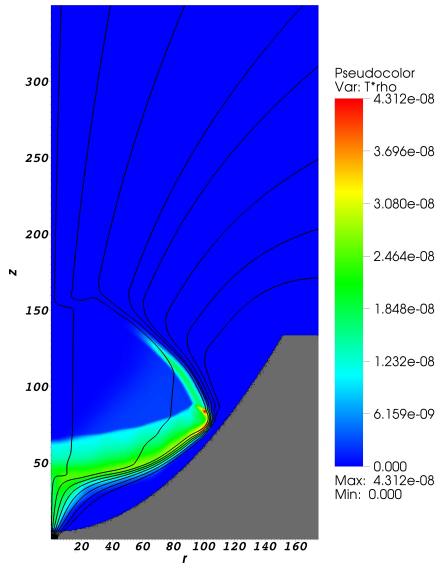


Figure B.18: $\mathcal{T} \cdot \rho$ profile and magnetic field lines at $t = 5.6\,\mu\text{s}$

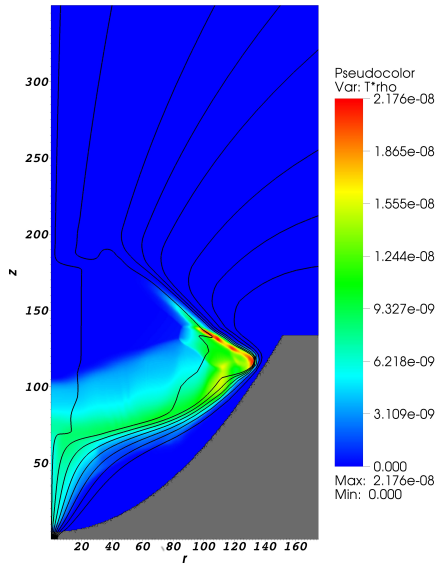


Figure B.19: $\mathcal{T} \cdot \rho$ profile and magnetic field lines at $t = 8.4\,\mu\text{s}$

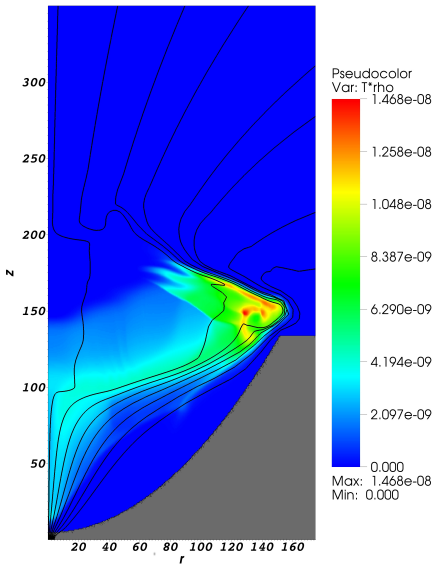


Figure B.20: $\mathcal{T} \cdot \rho$ profile and magnetic field lines at $t = 11.2\,\mu s$

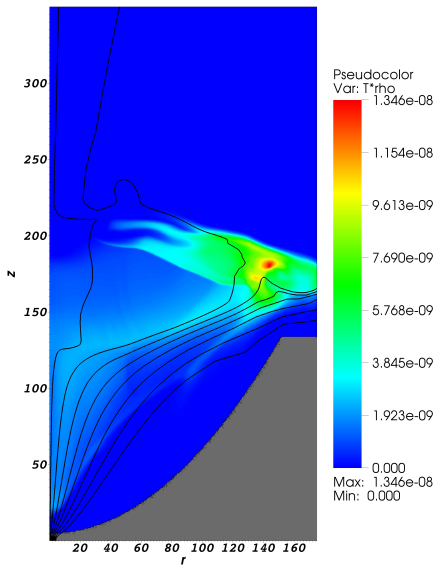


Figure B.21: $\mathcal{T} \cdot \rho$ profile and magnetic field lines at $t = 14\,\mu s$

## AppendixC. Nomenclature

*Roman Symbols*

$\boldsymbol{A}$: vector potential
$\boldsymbol{B}$: magnetic field vector
$B$: magnetic field magnitude
$e_f$: energy of the fusion reaction products
$e_{th}$: thermal energy
$e_{tot}$: total energy
$E$: complete elliptic integral of the second kind
$\boldsymbol{E}$: electric field vector
$\mathcal{E}$: electro motive force magnitude
$f_l$: focal length of the parabolic chamber
$\boldsymbol{F}$: flux tensor
$I$: electric current
$\boldsymbol{I}$: identity tensor
$k^2$: elliptic integral parameter
$K$: complete elliptic integral of the first kind
$m$: mass
$p$: momentum
$p_h$: hydrostatic pressure
$p_{tm}$: thermo-magnetic pressure
$q$: generic scalar variable
$r$: radial cylindrical coordinate
$R$: radius
$\boldsymbol{S}$: source term vector
$t$: time
$T$: thrust force
$\mathcal{T}$: tracer used as weighting factor
$\boldsymbol{U}$: vector of conservative variables
$\boldsymbol{v}$: velocity vector
$v$: scalar velocity
$v_A$: Alfvén speed
$z$: axial cylindrical coordinate

*Greek Symbols*

$\eta$: reaction chamber efficiency
$\rho$: mass density
$\phi$: azimuthal coordinate

*Subscripts*

0: initial conditions
$1, 2, ..., 8$: different values of the same variable
$f$: final conditions

$i$: ith computational cell
$n$: nth electric coil
$r$: radial component
$\phi$: azimuthal component
$z$: axial component

*Vector Calculus Symbols*

$\partial$: partial derivative operator
$\Delta$: discrete time variation of a physical quantity
$\boldsymbol{\nabla}\cdot$: divergence operator
$\boldsymbol{\nabla}\times$: curl operator
$\otimes$: tensor (outer) product

## AppendixD. Physical constants

$c \simeq 2.998 \cdot 10^8\,\mathrm{m/s}$: speed of Light
$g_0 \simeq 9.80665\,\mathrm{m/s^2}$: sea level Earth gravity acceleration
$\mu_0 = 4\pi \cdot 10^{-7}\mathrm{N/A^2}$: vacuum Permeability

## References


[1] S. C. Aleina, N. Viola, R. Fusaro, G. Saccoccia, Effective methodology to derive strategic decisions from ESA exploration technology roadmaps, Acta Astronautic. 126 (2016) 316 – 324, space Flight Safety. doi:http://doi.org/10.1016/j.actaastro.2016.05.012.
URL http://www.sciencedirect.com/science/article/pii/S0094576516300194

[2] C. Laurini, K., B. Hufenbach, J. Hill, A. Ouellet, The global exploration roadmap and expanding human/robotic exploration mission collaboration opportunities, in: Procedings of the 66th International Astronautical Congress, Jerusalem, Israel, 12-16 October, 2015.

[3] A. Rai, J. A. Robinson, J. Tate-Brown, N. Buckley, M. Zell, K. Tasaki, G. Karabadzhak, I. V. Sorokin, S. Pignataro, Expanded benefits for humanity from the international space station, Acta Astronautic. 126 (2016) 463 – 474, space Flight Safety. doi:http://doi.org/10.1016/j.actaastro.2016.06.030.
URL http://www.sciencedirect.com/science/article/pii/S0094576516301989

[4] L. Johnson, M. Meyer, B. Palaszewski, D. Coote, D. Goebel, H. White, Development priorities for in-space propulsion technologies, Acta Astronaut. 82 (2012) 148–152. doi:10.1016/j.actaastro.2012.05.006.

[5] J. Cassibry, R. Cortez, M. Stanic, A. Watts, W. Seidler, II, R. Adams, G. Statham, L. Fabisinski, Case and Development Path for Fusion Propulsion, J. of Spacecr. and Rockets 52 (2015) 595–612. doi:10.2514/1.A32782.

[6] Human exploration of mars: Design reference architecture 5.0, Tech. Rep. SP–2009–566, NASA (2009). doi:10.1109/AERO.2010.5446736.

[7] F. Romanelli, C. Bruno, Assessment of open magnetic fusion for space propulsion, in: Proceedings of the 57th International Astronautical Congress, Valencia, Spain, 12-16 October, 2006. doi:10.2514/6.IAC-06-C4.6.02.

[8] R. L. Clark, R. B. Sheldon, Dusty plasma based fission fragment nuclear reactor, in: Proceedings of the 41st Joint Propulsion Conference and Exhibit, Tucson, AZ, USA, 10-13 July, 2005. doi:10.2514/6.2005-4460.

[9] R. A. Gabrielli, D. Petkow, G. Herdrich, R. Laufer, H.-P. Röser, Two generic concepts for space propulsion based on thermal nuclear fusion, Acta Astronaut. 101 (2014) 129–137. doi:10.1016/j.actaastro.2014.03.015.

[10] F. Winterberg, To mars in weeks by thermonuclear microbomb propulsion, J. of Propuls. and Power 30 (6) (2014) 1480–1484.

[11] F. Winterberg, Deuterium–tritium pulse propulsion with hydrogen as propellant and the entire space-craft as a gigavolt capacitor for ignition, Acta Astronautica 89 (2013) 126 – 129. doi:http://doi.org/10.1016/j.actaastro.2013.04.004.
URL http://www.sciencedirect.com/science/article/pii/S0094576513001161

[12] J. Slough, A. Pancotti, D. Kirtley, C. Pihl, M. Pfaff, Nuclear propulsion through direct conversion of fusion energy: The fusion driven rocket, Tech. rep., MSNW LLC (2012).

[13] T. Polsgrove, R. B. Adams, L. Fabisinski, S. Fincher, , C. D. Maples, T. Miernik, Janie ad Percy, G. Statham, M. Turner, J. Cassibry, R. Cortez, J. Santarius, Z-pinch pulsed plasma propulsion technology development final report, Tech. Rep. M11-0145, NASA Marshall Space Flight Center; Huntsville, AL, USA (2010).

[14] C. D. Orth, Vista – a vehicle for interplanetary space transport application powered by inertial confinement fusion, Tech. Rep. Ucrl-Tr-110500, Lawrence Livermore National Lab., Livermore, CA, USA (2003).

[15] Y. C. F. Thio, R. Freeze, R. Kirkpatrick, B. Landrum, H. Gerrish, G. Schmidt, High-energy space propulsion based on magnetized target fusion, in: Proceedings of the 35th Joint Propulsion Conference and Exhibit, Los Angeles, CA, USA, 20-24 June, 1999. doi:10.2514/6.1999-2703.

[16] F. Winterberg, Rocket propulsion by thermonuclear microbombs ignited with intense relativistic electron beams, Raumfahrtforsch. 15 (1971) 208–217.

[17] J. Miernik, G. Statham, L. Fabisinski, C. D. Maples, R. Adams, T. Polsgrove, S. Fincher, J. Cassibry, R. Cortez, M. Turner, T. Percy, Z-Pinch fusion-based nuclear propulsion, Acta Astronaut. 82 (2013) 173–182. doi:10.1016/j.actaastro.2012.02.012.

[18] A. Bond, Project Daedalus Study Group, Project Daedalus: The Final Report on the BIS Starship Study, Vol. 31 (Suppplement), J. Brit. Interplanet. Soc., 1978.

[19] R. B. Adams, R. A. Alexander, J. M. Chapman, S. S. Fincher, R. C. Hopkins, A. D. Philips, T. T. Polsgrove, R. J. Litchford, B. W. Patton, G. Statham, P. S. White, Y. C. F. Thio, Conceptual design of in-space vehicles for human exploration of the outer planets, Tech. Rep. TP—2003–212691, NASA (2003).

[20] G. Romanelli, Pulsed fusion space propulsion: Computational ideal magneto-hydro dynamics of a magnetic flux compression reaction chamber, Master's thesis, TU Delft (2016).

[21] P. Turchi, P. Mikellides, R. Gerwin, P. Gessini, Numerical simulation of magnetic nozzle flow for nuclear fusion space propulsion, in: Proceedings of the 35$^{\text{th}}$ Joint Propulsion Conference and Exhibit, Los Angeles, CA, USA, 20-24 June, 1999.

[22] F. H. Ebersohn, Gas kinetic study of magnetic field effects on plasma plumes, Master's thesis, Texas A&M University (2012).

[23] M. Stanic, J. T. Cassibry, R. B. Adams, Project icarus: Analysis of plasma jet driven magneto-inertial fusion as potential primary propulsion driver for the icarus probe, Acta Astronaut. 86 (2013) 47–54. doi:10.1016/j.actaastro.2012.08.010.

[24] A. Mignone, G. Bodo, S. Massaglia, T. Matsakos, O. Tesileanu, C. Zanni, A. Ferrari, Pluto: a numerical code for computational astrophysics, The Astrophys. J. Suppl. Ser. 170 (2007) 228–242. doi:10.1086/513316.

[25] E. F. Toro, Riemann Solvers and Numerical Methods for Fluid Dynamics, Springer, 2009. doi:10.1007/b79761.

[26] H. Childs, E. Brugger, B. Whitlock, J. Meredith, S. Ahern, D. Pugmire, K. Biagas, M. Miller, C. Harrison, G. H. Weber, H. Krishnan, T. Fogal, A. Sanderson, C. Garth, E. W. Bethel, D. Camp, O. Rübel, M. Durant, J. M. Favre, P. Navrátil, VisIt: An End-User Tool For Visualizing and Analyzing Very Large Data, in: High Performance Visualization–Enabling Extreme-Scale Scientific Insight, 2012, pp. 357–372.

[27] J. C. Simpson, J. E. Lane, C. D. Immer, R. C. Youngquist, Simple analytic expressions for the magnetic field of a circular current loop, Tech. Rep. TM-2013-217919, NASA (2001).

[28] P. G. Mikellides, P. J. Turchi, N. F. Roderick, Applied-field magnetoplasmadynamic thrusters, part 1: Numerical simulations using the mach2 code, J. of Propuls. and Power 16 (5) (2000) 887–893.

[29] J. D. Jackson, Classical Electrodynamics, 3rd Edition, Wiley, 1998. doi:10.1119/1.19136.

[30] A. Chambers, Modern Vacuum Physics, 1st Edition, CRC Press, 2004.

[31] F. H. Ebersohn, B. W. Longmier, J. V. Shebalin, Mhd simulation of plasma rocket exhaust, in: Proceedings of the 9$^{\text{th}}$ PAMIR International Conference on Fundamental and Applied MHD, Riga, Latvia, 16-20 June, 2014.

[32] I. G. Mikellides, P. J. Turchi, T. M. York, Rocket propulsion by thermonuclear microbombs ignited with intense relativistic electron beams, J. of Propuls. and Power 18 (1) (2002) 152–158.

**Vitae**

Gherardo Romanelli attained a BSc degree in Aerospace Engineering at University of Pisa (Italy) and a MSc degree in Space Systems Engineering at Delft University of Technology (The Netherlands). The objective of his master's thesis project was that of contributing to the advancement of manned space exploration capabilities and its results were presented at the $67^{th}$ IAC in Guadalajara. This is his first publication in an international journal after that in the conference proceedings of the IAC.

Angelo Cervone is Assistant Professor in the Aerospace Engineering Faculty at Delft University of Technology. He holds a PhD in aerospace propulsion from University of Pisa (Italy), followed by a 2-years post-doc at Osaka University (Japan). His main research areas are space propulsion, micro-propulsion systems for small satellites, flow instabilities in space rocket turbopumps, systems engineering. He is actively involved in the education curricula of the faculty, where he teaches several courses with large use of innovative education techniques such as blended learning and online lecturing. He is co-author of more than 100 papers in international journals and conference proceedings.

Andrea Mignone received his PhD in astrophysics in 2004 at the University of Chicago (Illinois,USA) and has been actively working in the field of computational astrophysics for more than 15 years. Currently, he is an associate professor at the Physics Department, University of Turin (Italy) where he is teaching Plasma Physics and Numerical methods for Physics. His research activities involve large-scale computations of astrophysical flows and the development of the PLUTO code for magnetohydrodynamics and plasma physics.